The Elastic Properties and Anisotropic Behavior of $MgSiO_3$ Akimotoite at Transition Zone Pressures

N. C. Siersch[1, *], A. Kurnosov[1], G. Criniti[1], T. Ishii[1], T. Boffa Ballaran[1] and D. J. Frost[1]

[1] Bayerisches Geoinstitut, Universität Bayreuth, D-95440 Bayreuth, Germany.

*Corresponding author: Nicki C. Siersch (nicki.siersch@upmc.fr), present address: Institut de Minéralogie, de Physique des Matériaux et de Cosmochimie (IMPMC), Sorbonne Université, UMR CNRS 7900, IRD, Muséum National d'Histoire Naturelle, F-75005 Paris, France.

(Accepted for publication in Physics of the Earth and Planetary Interiors, November 2021)

Abstract

Seismic wave velocities in the Earth's transition zone, between 410 and 660 km depth, are poorly matched by mineralogical models. Mainly due to the presence of majoritic garnet, wave velocities calculated for a peridotite composition lithology are slower than seismic reference models, particularly towards the base of the transition zone. One possible resolution for this is if the $MgSiO_3$ polymorph akimotoite replaces majoritic garnet in some regions of the transition zone, which occurs in peridotitic material if temperatures are slightly lower than a typical geotherm or in harzburgitic composition material. Its presence might serve as an explanation not only for the discrepancy of seismic velocities at the base of the transition zone but also for observations of transition zone seismic anisotropy in regions of current subduction. In order to provide the data required to test this possibility, two high-quality single-crystals of $MgSiO_3$ akimotoite were studied using combined Brillouin spectroscopy and X-ray diffraction up to 24.86(3) GPa, i.e. to the limit of the akimotoite stability field. The resulting equation of state yields an adiabatic bulk modulus and first pressure derivative of K_{S0} = 209(2) GPa and K' = 4.4(1), respectively, and a shear modulus and first pressure derivative of G_0 = 131(1) and G′ = 1.7(1). This is in overall agreement with several experimental and computational studies, however, the resulting aggregate velocities are slower than previously reported, especially at high pressures. The elastic anisotropy of akimotoite is found to decrease only slightly with pressure; akimotoite hence remains the most elastically anisotropic mineral in the transition zone and may therefore play a major role in explaining seismic anisotropy observations in the proximity of subducting slabs.

Keywords: Akimotoite, elasticity, anisotropy, Brillouin spectroscopy, high-pressure, transition zone

1 Introduction

The Earth's transition zone between 410 and 660 km depth is of particular interest since it marks a region of transitional seismic wave velocities that arises due to pressure induced mineral phase transitions. Mineralogical models for a peridotitic bulk mantle composition are not in good agreement with seismic reference models for transition zone seismic velocities (Dziewonski and Anderson, 1981; Kennett et al., 1995), particularly at its base, since the elastic parameters of the two main minerals stable at these conditions, ringwoodite and majoritic garnet, give rise to slower compressional and shear wave velocities (Irifune et al., 2008; Pamato et al., 2016). Several tomographic studies have reported the stagnation and accumulation of slab material at the 660 km-discontinuity that could significantly lower the average temperature in some areas relative to the mantle geotherm (e.g. Fukao et al., 2009, 2001; Fukao and Obayashi, 2013; Van Der Hilst et al., 1991). Lower temperatures would correspond to high wave velocities in mineralogical models that may well produce a better fit to the global seismic reference models. However, in this cooler environment, majoritic garnet may be partially replaced by akimotoite (Gasparik, 1990; Hirose, 2002; Ishii et al., 2011; Kato, 1986; Ohtani et al., 1991; Sawamoto, 1987), a $MgSiO_3$ polymorph that crystallizes in the trigonal system with space group $R\bar{3}$ and which is stable between 18 and 25 GPa and 900 to 2200 K. An even greater proportion of akimotoite would be formed within harzburgitic compositions that might result from the accumulation of subducted lithospheric mantle at the base of the transition zone (Irifune and Ringwood, 1987; Zhang et al., 2013; Ishii et al., 2019). Harzburgitic material may also be present above subducting slabs as residues of sub arc melting are dragged into the subduction zone.

In spite of the potential importance of this mineral, very few studies have been focused on constraining its elastic behavior. Only one experimental study, to date, has examined the full elastic tensor of $MgSiO_3$ akimotoite at room pressure and temperature (Weidner and Ito, 1985). This previous Brillouin spectroscopy study is the only elasticity measurement performed on an akimotoite single-crystal. Two studies have examined akimotoite compressibility using polycrystalline samples; one at room temperature using a diamond anvil cell (DAC) up to 28 GPa, with H_2O as the pressure transmitting medium (Reynard et al., 1996), and the other using

a large volume press and synchrotron radiation up to 19 GPa and 1373 K (Wang et al., 2004). Both of these studies, however, fixed the value of the akimotoite bulk modulus, K_{T0}, to the value reported by Weidner and Ito (1985) and fitted only the first pressure derivative of the bulk modulus, K'_{T0} . A more recent study (Zhou et al., 2014) successfully determined both bulk and shear moduli of $MgSiO_3$ akimotoite by means of ultrasonic measurements performed in a multianvil apparatus on a polycrystalline akimotoite sample up to the actual stability field of akimotoite, 25.7 GPa and 1500 K. Some discrepancies exist, however, between the multianvil experiments of Zhou et al. (2014) and previous compression, Brillouin and computational (Da Silva et al., 1999; Hao et al., 2019) studies (Table 1). Computational and experimental studies agree, however, that the wave velocities of akimotoite are faster than those expected for majoritic garnet (Pamato et al., 2016) and ringwoodite (Schulze et al., 2018). The presence of akimotoite might, therefore, bring mineralogical models for the seismic velocities of mantle compositions at the base of the transition zone into agreement with the predictions of seismic reference models, if the discrepancies in elastic properties observed between previous studies can be resolved.

Insert Table 1

The potential presence of akimotoite in subducted lithospheric mantle may also be a consideration when trying to explain observations of seismic anisotropy in the lower part of the transition zone and upper part of the lower mantle. The base of the transition zone should be nearly isotropic because the dominant minerals, ringwoodite and majoritic garnet, display little to no elastic anisotropy (e.g. Mainprice, 2015). However, studies of normal modes and surface waves (Montagner and Kennett, 1996; Trampert and Van Heijst, 2002; Yuan and Beghein, 2013) as well as of source-side wave splitting (Nowacki et al., 2015) show varying degrees of anisotropy in the transition zone and upper lower mantle around subduction zones. Akimotoite is a highly anisotropic mineral at room pressure (Weidner and Ito, 1985) and ab initio simulations and molecular dynamics studies (Da Silva et al., 1999; Hao et al., 2019; Zhang et al., 2005) show that this anisotropy is still pronounced at high-pressures and temperatures. Zhang et al. (2005) incorporated the calculated anisotropy of akimotoite into a modelled phase assemblage consisting of akimotoite, ringwoodite and Ca-perovskite and found that the overall wave velocity anisotropy, albeit smaller, had the same anisotropic features of those reported for akimotoite. Shiraishi et al. (2008) investigated the crystallographic preferred orientation (CPO) of akimotoite recovered from deformation experiments at high pressures and temperatures. They observed a change in CPO pattern with temperature at a given pressure, which may

explain the anisotropic features observed in the Northern and Southern segments of the Tonga slab. However, their results are only qualitative, given that they used the elastic tensor of akimotoite measured at room pressure (Weidner and Ito, 1985) to explain the akimotoite CPO. In fact, no experimental constraints on the variation of the elastic tensor with pressure exist to date. The discrepancy between aggregate wave velocities calculated from ab initio simulations (Da Silva et al., 1999; Hao et al., 2019) and those obtained from ultrasonic measurements (Zhou et al., 2014), means that some uncertainty remains as to the extent of anisotropy of akimotoite at pressures of the transition zone.

In this study the full elastic tensor of $MgSiO_3$ akimotoite has been obtained up to ~25 GPa by means of Brillouin spectroscopy and single-crystal X-ray diffraction. The stiffness coefficients have then been used to calculated both aggregate velocities and the anisotropy behavior of akimotoite as a function of pressure. The use of a single-crystal under quasi-hydrostatic conditions has the advantage of avoiding any preferred orientation, which may arise in powdered samples, and thus provides strong constraints for the ultimate interpretation of regions of the transition zone exhibiting seismic anisotropy. By performing measurements to that determine elastic moduli and density simultaneously, absolute pressure determinations can be made without the need for secondary pressure standards.

2 Methods

2.1 Sample synthesis and characterization

The starting material for synthesizing large $MgSiO_3$ akimotoite single-crystals was produced by mixing two synthetic oxides MgO and SiO_2 in 1:1 proportion and grinding them under ethanol for 1 h to obtain a homogeneous mixture. This mixture was then placed into a Pt crucible and heated in a high-temperature furnace up to 1600 °C where it was kept for 3 h. The starting material was then rapidly quenched in an icy water bath to obtain a glass. The glass was ground again for 1h under ethanol and heated at 1200 °C for 2 h to crystallize enstatite. The crystallized starting material was further mixed with 15 wt.% excess MgO to avoid the growth of stishovite crystals when silicate is dissolving incongruently in the solvent material as reported by Shatskiy et al. (2007). The starting mixture was filled into a 3.5 mm long Pt capsule and a drop of H_2O was added as flux material to enhance crystal growth. The Pt capsule was welded carefully with a Lampert PUK U3 welding device in micro mode (power: 7 %, time: 3-

5 ms) to prevent the leakage of the solvent or melt produced during the experiment. A 10/4 assembly was used consisting of a 10 mm edge-length MgO octahedron doped with Cr_2O_3 acting as pressure medium and 4 mm truncated WC anvils. The Pt capsule was placed into a MgO sleeve to separate the sample from the $LaCrO_3$ furnace. In addition, a ZrO_2 sleeve was placed between the $LaCrO_3$ heater and the octahedron acting as a thermal insulator. No thermocouple was used due to the length of the Pt capsule; however, a reliable power-temperature relationship was used from previously conducted experiments performed at exactly the same *P-T* conditions. The synthesis experiment was performed at 22 GPa and ~1600 °C (estimated from a power-temperature relationship) in the 1200t Sumitomo split-sphere multi-anvil apparatus at the Bayerisches Geoinstitut, University of Bayreuth and was heated for 4 h, followed by quenching and slow decompression. The recovered capsule was carefully opened revealing a mixture of crystallized melt together with crystals up to 500 µm in size. The akimotoite crystals were characterized using a LEO 1530 scanning electron microscope (SEM) operated at 20 kV in order to observe the possible presence of stishovite inclusions inside the crystals. Quantitative chemical analyses were performed on a JEOL JXA-8200 electron microprobe (EMP) operating at 15 kV and 15 nA with a focused beam. Sample and background were collected for 20 s and 10 s, respectively. Enstatite was used as a standard for both Mg and Si. Fourier-transform infrared spectroscopy (FTIR) measurements on one single-crystal oriented parallel to the (100) plane and polished to a thickness of 59 µm were performed to investigate its possible water content. The measurement was performed using a Bruker IFS 120 high-resolution FTIR Spectrometer coupled with a Bruker A490 IR microscope. A tungsten light source was used in combination with a CaF_2 beam splitter coated with Si and a high-sensitivity, narrow-band MCT detector. An aperture of 0.45 mm at 15x magnification produced a spot size of 30 µm on the measured sample. The spectral range between 2500 to 5000 cm^{-1} has been investigated with 1000 scans of 4 cm^{-1} resolutions. One unpolarized and two polarized FTIR spectra, one parallel to the *c*-axis and one perpendicular to the *c*-axis, were collected (Figure S1). The true thickness of the polished crystal used for the measurements was measured using the optical microscope calibrated with a metal foil reference. The collected absorbance FTIR spectra were corrected using as baseline a spline fit through points outside the OH band region. The hydroxyl concentration was then calculated by numerical integrating the baseline-corrected absorbance bands using the calibration reported by Paterson (1982):

158 $$C_{OH} = \frac{X_i}{150\zeta} \int \frac{K(\tilde{\nu})}{(3780 - \tilde{\nu})} d\tilde{\nu}$$

159

160 where X_i =2361 ppm wt H_2O is the density factor for $MgSiO_3$-akimotoite (Bolfan-Casanova et
161 al., 2000), ζ is an orientation factor and $K(\tilde{\nu})$ is the absorption coefficient for a given
162 wavenumber $\tilde{\nu}$. For uniaxial minerals the orientation factor ζ is equivalent to $c_{OH} = 2c_\omega + c_\varepsilon$
163 where c_ω and c_ε are the concentrations measured perpendicular and parallel to the *c*-axis of
164 akimotoite (see for details Bolfan-Casanova et al. 2000). The FTIR measurements resulted in a
165 hydroxyl content of 281 ppm wt. H_2O. This fairly negligible amount of water is in agreement
166 with the results reported by Bolfan-Casanova et al. (2000) who measured between 351(25) ppm
167 and 425 ppm wt. H_2O in akimotoite single-crystals synthesized in water saturated environments
168 at temperatures between 1573 and 1873 K and pressures between 19 and 24 GPa.

169

170 2.2 Sample preparation for high-pressure experiments

171 Three large (~100-200 µm) single-crystals of akimotoite (X1, X2 and X3) were selected
172 based on their sharp diffraction profiles (full width at half maximum in omega scans less than
173 0.08°) using an Oxford Diffraction Xcalibur diffractometer equipped with MoKα radiation (λ
174 = 0.70937 Å) operated at 50 kV and 40 mA, a graphite monochromator and a Sapphire 2 CCD
175 area detector and a Huber four-circle Eulerian cradle diffractometer equipped with an
176 unmonochromated Mo radiation source operated at 50 kV and 40 mA and a point detector. The
177 crystals were oriented on three different planes, i.e. (0.43 -3.28 8.91) for X1, (-3.08 4.60 -2.36)
178 for X2 and (0 0 1) for X3 and double-sided polished to a thickness of 15(1) µm. The polished
179 crystals were then cut into half circles of 88 - 90 µm in diameter using a Focused Ion Beam
180 machine FEI Scios DualBeam equipped with a Ga^+ ion beam at 20 kV and 0.80 nA. Crystals
181 X1 and X2 were loaded together (inset in Figure 1) into a BX90 style diamond anvil cell (DAC)
182 (Kantor et al., 2012) using diamonds with 400 µm culet size glued into Boehler-Almax seats
183 having an opening angle of 90°. A Re gasket was pre-indented to a thickness of ~ 60 µm and a
184 hole with a diameter of 230 µm was laser-cut into the center of the indentation. A small ruby
185 sphere was placed next to the crystals for use as a pressure marker during the experiment, for
186 which the ruby fluorescence pressure calibration reported by Dewaele et al. (2004) was used.
187 Neon was gas-loaded as a quasi-hydrostatic pressure transmitting medium (Kurnosov et al.,
188 2008). After each pressure increase the DAC was left to stabilize for at least one day to avoid

any pressure changes during the XRD and Brillouin measurements. In addition, the ruby fluorescence was measured before and after each XRD and Brillouin measurement using a Raman micro-spectrometer equipped with a He-Ne-laser (λ = 632.8 nm) with 20 mW laser power. Crystal X3 was measured by means of Brillouin spectroscopy only at room conditions.

2.3 High-pressure experiments

Simultaneous high-pressure single-crystal X-ray diffraction and Brillouin spectroscopy measurements were performed using an in-house BGI facility. This consists of a Huber four-circle Eulerian cradle diffractometer with a point detector coupled with a MoKα rotating anode Rigaku X-ray source equipped with a VaryMax focusing optic (Trots et al., 2011) and a Brillouin system comprising a 532 nm solid-state laser, a multi-pass tandem Fabry-Pérot interferometer and a Hamamatsu single photon counting module H11202-050 (Trots et al., 2013). Nine individual Bragg reflections were collected for each crystal using the eight-position centering method (King and Finger, 1979) implemented in the SINGLE software (Angel and Finger, 2011). The unit-cell lattice parameters (Table 2) were obtained at 13 pressure points up to 12.1(1) GPa in a first experiment (DAC1). The experiment was then interrupted due to broadening of the Bragg reflections of crystal X2. In a second experiment (DAC2), the unit-cell lattice parameters were measured at 14 pressure points up to 24.9(1) GPa (Table 2). A slight broadening of the Bragg reflections was observed for both crystals above 14 GPa, therefore the DAC was placed on a heating plate at 200 °C for 30 minutes. The pressure inside the DAC dropped to ~11 GPa, and the reflections became sharper again and remained sharp until the maximum pressure was reached.

Insert Table 2

Brillouin spectra for crystals X1 and X2 were collected at eleven pressure points up to 24.9(1) GPa, whereas at room conditions Brillouin spectra were collected separately for crystals X1 and X3. Twenty different chi orientations were measured at each pressure point and for each sample. A Brillouin spectrum collected at 4 GPa for crystal X2 is shown in Figure 1 as an example. Note that the signals from the neon pressure transmitting medium are also present together with the longitudinal, v_P and two shear, v_{S1} and v_{S2}, acoustic wave velocities of the akimotoite crystal. With increasing pressure, the longitudinal signal of akimotoite approached the large secondary signal of the diamond, thus, an aperture mask (width: 5 mm) was used to

filter out the tails of the diamond peaks to allow the observation of the sample signals at higher pressures. Each spectrum was collected for at least 30 min and up to 12 hours, depending on the orientation of the sample and the signal to noise ratio. The measured frequency shifts were directly converted into acoustic wave velocities using the calibration obtained at ambient conditions from the measurement of a fused silica standard. The Brillouin signals were analyzed using the program Brillouin Win1024 version 2.6.3 written by S. Sinogeikin. The seven independent stiffness coefficients of akimotoite expressed in Voigt notation, c_{11}, c_{33}, c_{44}, c_{12}, c_{13}, c_{14}, c_{25}, were obtained by fitting the variation with azimuthal chi angle of the three acoustic velocities at each pressure point using the Christoffel equation $\left|c_{ijkl}q_j q_l - \rho v^2 \delta_{ik}\right| = 0$ with c_{ijkl} being the elastic coefficients, $q_{j,l}$ the crystallographic orientation of each single-crystals, ρ the density obtained by means of X-ray diffraction and δ_{ik} the Kronecker delta. The absolute pressure could be calculated since density and the adiabatic bulk modulus are determined simultaneously by X-ray diffraction and Brillouin spectroscopy, respectively, without having to rely on the pressure determined from a secondary pressure gauge, as the ruby sphere used in this study. The absolute pressure was calculated according to:

$$P_{abs} = -\int_{V_0}^{V} \frac{K_T(V)}{V} dV = 3K_{T0} f(1+2f)^{\frac{5}{2}}\left(1+\frac{3}{2}(K'_{T0}-4)f\right)$$

with

$$f = \frac{1}{2}\left[\left(\frac{V_0}{V_P}\right)^{\frac{2}{3}} - 1\right]$$

and transforming the adiabatic bulk modulus obtained from Brillouin spectroscopy to isothermal according to the $K_{S0} = K_{T0} * (1 + \alpha\gamma T)$ with α = 2.44x10^{-5} 1/K (Ashida et al., 1988), γ = 1.18 (Stixrude and Lithgow-Bertelloni, 2005) and T = 298 K. A comparison between the absolute pressure and the pressures determined from the ruby fluorescence shift using the calibration reported by Dewaele et al. (2004) is plotted in Figure S2. The two pressures are in agreement within 2.5 % uncertainty of the ruby pressure scale up to 25 GPa. The fitting procedure is implemented into an Origin 2018 program as described in details by Buchen (2018). The elastic tensor of akimotoite (Table 3) was then used in the software package Anis2k (Mainprice, 1990) to calculate the distribution of the velocity anisotropies for P and S-waves up to pressures of the Earth's transition zone.

Insert Figure 1 and Table 3

3 Results and Discussion

3.1 Compressibility of $MgSiO_3$ akimotoite

The variation with pressure of the unit-cell lattice parameters and volumes (Table 2) normalized with respect to their measured room pressure values are reported for both crystals investigated in this study in Figures 2a and b. $MgSiO_3$ akimotoite is much more compressible along the *c*-axis giving rise to a very anisotropic axial compressibility. A Birch-Murnaghan third-order equation of state (BM3 EoS) has been used to fit the *P*-*V* data of both crystals using the EoSFit7GUI program (Angel et al., 2014). The resulting EoS parameters are, V_0 = 262.43(2) Å^3, K_{T0} = 205(1) GPa and K' =4.9(2) (Table 1). Linearized BM3 EoS have been used to fit the variation of the *a*- and *c*-axes with pressure and the resulting EoS parameters are: a_0 = 4.7277 (2) Å, M_{0a} = 728 (6) GPa, M_{0a}' = 16.0 (7) and c_0 = 13.5580 (3) Å, M_{0c} = 470 (2) GPa, M_{0c}' = 12.6 (3). As expected, the axial modulus for the *a*-axis is much larger than that obtained for the *c*-axis, however, the anisotropy in axial compressibility decreases slightly with pressure (Figure S3), in agreement with the elastic anisotropy, as discussed later.

Insert Figure 2a and b

The unit-cell lattice parameters reported by Reynard et al. (1996), Wang et al. (2004) and Zhou et al. (2014) normalized with respect to their corresponding room pressure values are compared to the single-crystal akimotoite data obtained in the present study in Figure 2. The compressibilities of the *a*-axis reported by Reynard et al. (1996) and Wang et al. (2004) are stiffer than the compressibility found in this study (Figure 2a). The *c*-axis reported by Wang et al. (2004) is, however, more compressible than the one found in this study leading to a comparable compressibility of the volume data (Figure 2b). The compressibility of the *c*-axis reported by Reynard et al. (1996) instead is comparable to that described in this study, which, combined with the stiffer *a*-axis, leads to an overall stiffer volume compressibility (Figure 2b). It is likely that non-hydrostatic stresses were developed inside the DAC experiment of Reynard et al. (1996) due to the use of H_2O as pressure transmitting medium, which transforms to ice VII above 2.5 GPa and may, therefore, produce non-hydrostatic conditions above this pressure (Angel et al., 2005). The *P*-*V* data reported by Reynard et al. (1996) and Wang et al. (2004) can be refitted using a 2nd-oder Birch-Murnagham (BM2) EoS, with K' fixed to 4, using the

EoSfitGUI software (Angel et al., 2014), to account for the fact that in these two studies K_{T0} had been fixed to the value reported by Weidner and Ito (1985). Fixing the bulk modulus values in this way will strongly bias the value of K' determined due to the large correlations between these two parameters. Due to the data scatter, it was not possible to fit a BM3 to the literature data, further suggesting that the values of K' cannot be constrained from these experiments. The refitted K_{T0} = 212(15) GPa, (Table 1), for the data of Wang et al. (2004) is slightly larger than the value obtained in this study whereas the refitted value for the data of Reynard et al. (1996) is the largest, K_{T0} = 228(8) GPa, as expected due to the stiffer behavior observed. The volume data reported by Zhou et al. (2014) are in good agreement with the data collected in this study, although a larger value of K_{S0} and a smaller K' (Table 1) are found, arising from the relatively high values of v_P collected in their ultrasonic experiments (see next section).

3.2 Wave velocities of $MgSiO_3$ akimotoite

The c_{ij} coefficients (Table 3) obtained at ambient pressure are in good agreement with the c_{ij} determined by Weidner and Ito (1985) (Figure S4), although the values of c_{11}, c_{33} and c_{12} are between 3% and 9% larger than the values obtained in this study. Note, moreover, that the c_{14} reported in this study is positive whereas that reported by Weidner and Ito (1985) is negative. This is most likely due to a different setting used for the transformation from the trigonal system of akimotoite to the orthogonal system used to describe the acoustic wave velocity directions. Weidner and Ito (1985) do not report which setting they have used, but from the analysis of the velocity anisotropy (see next section), it is very likely that these authors have chosen the crystallographic *a*-axis to be parallel the orthogonal X-axis, whereas in this study we have chosen the a^* to be parallel to X. Most of the stiffness coefficients increase monotonously with increasing density (Figure S4), except for c_{14} and c_{25}, which decrease with pressure.

Knowledge of the compliance tensor s_{ij}'s, obtained through inverting the elastic tensor, allows the calculation of the axial compressibility β according $\beta_1 = s_{11} + s_{12} + s_{13}$ and $\beta_3 = s_{31} + s_{32} + s_{33}$ where β_1 and β_3 are the axial compressibility for the *a*- and *c*-axis, respectively. This can be directly compared to the linear compressibility obtained by X-ray diffraction (see section 3.1) following $\beta = \frac{1}{M}$. The compressibility for both the *a*- and *c*-axes determined independently from the two different methods are shown in Figure S3 and are in excellent agreement.

The Reuss and Voigt bounds (Nye, 1985) of the bulk and shear moduli were calculated using the c_{ij}'s and the compliance coefficients s_{ij}'s are shown in Figure 3 as a function of density. As proposed by (Watt et al., 1976), the arithmetic average has been used to calculate the Reuss-Voigt-Hill average (Hill, 1952), which represents the aggregate bulk and shear moduli of a composite material. These values are also indicated in Figure 3 (black symbols). The adiabatic bulk modulus of 208(1) GPa obtained from Brillouin spectroscopy is in excellent agreement with the adiabatic bulk modulus calculated from the isothermal bulk modulus obtained from fitting the *P*-*V* data (see Table 1 for details).

Insert Figure 3

The aggregate compressional and shear wave velocities, were calculated following the Adams-Williamson relations $v_P = \sqrt{\frac{K+4/3G}{\rho}}$ and $v_S = \sqrt{\frac{G}{\rho}}$, respectively, by using the elastic moduli determined with the Reuss-Voigt-Hill average and density measured using single-crystal X-ray diffraction on the same crystals (Figure 4). The difference between the Reuss and Voigt bounds for both the longitudinal and shear wave velocities are ~0.3 km/s and decrease slightly with increasing pressure indicating a decrease in anisotropy (Figure 4). The values obtained by Weidner and Ito (1985) (blue triangles in Figure 4) are slightly faster than the RVH average velocities determined in this study as expected from the larger values for their c_{11}, c_{33} and c_{12} coefficients (Figure S4). The shear wave velocities (green circles in Figure 4) obtained by Zhou et al. (2014) by means of ultrasonic measurements are in agreement with those reported in this study at pressures below 17 GPa, but become faster at higher pressure due to their larger pressure derivative. Moreover, the v_P reported in this previous study have not only a steeper slope but are faster at all pressures and even exceed the Voigt bound determined in this study (Figure 4). The discrepancy could be due to the presence of preferential orientation in the polycrystalline sample of Zhou et al. (2014), evolved either during synthesis or during the high-pressure heating cycles as ultrasonic measurements were performed. This would require the akimotoite crystals to be preferentially aligned with the *a*-axis along the wave propagation direction, since v_P would then be faster but the summation of v_{S1} and v_{S2} in the basal plane would lead to very little effect on the aggregate v_S (see Figure S5). Note that this would actually be consistent with crystal preferred orientation study of Shiraishi et al. (2008) who report that akimotoite crystals deformed at temperatures below 1273 K indeed have the *c*-axis oriented perpendicular to the compression direction. Da Silva et al. (1999) conducted a computational study on $MgSiO_3$ akimotoite using the ab initio pseudo-potential method and obtained

longitudinal and shear wave velocities (purple lines in Figure 4) which lie very close to the Voigt bound of the current study. Their pressure dependence is not as steep as that shown in the current study, moreover, the room pressure bulk and shear moduli reported by Da Silva et al. (1999) are much larger (Table 1), likely due to the fact that the study has been performed at 0 K. A very recent study (Hao et al., 2019) (pink lines in Figure 4) used density functional theory to compute the elastic parameters of akimotoite up to 30 GPa and 2000 K and reported a K_{T0} = 202 GPa and G_0 = 126 GPa at 298 K (Table 1) resulting in v_P and v_S that are slower than those experimentally determined in this study and close to the Reuss bound at pressures consistent with akimotoite stability.

Insert Figure 4

3.3 Anisotropic behavior of $MgSiO_3$ akimotoite at transition zone pressures

The velocity distributions along the different propagation directions for akimotoite at room pressure and at 24.9(1) GPa are shown in Figures S3 and S4. In comparison to the velocity distribution determined in this study, the ones obtained using the elastic coefficients by Weidner and Ito (1985) are rotated clockwise by 30° as expected given the different crystallographic setting used (Figure S5, right) as described above. The fastest velocities do not travel along the crystallographic axes, in fact they lie inclined relative to the (001) and (100) planes. Among the slowest velocities, only v_{S2} travels along the crystallographic *c*-axis. In the (001) plane perpendicular to the *c*-axis, the v_P velocities vary very little at room pressure, whereas in the same plane the Av_{SP} is very large. These results are in agreement with a molecular dynamics study of Zhang et al. (2005) and with the ab-initio study of Da Silva et al. (1999). With increasing pressure to 25 GPa, the difference between the maximum and minimum velocities decrease gradually, however, the overall distribution of the fastest and slowest velocities as well as the anisotropies remains the same (Figures S3 and S4). This in excellent agreement with the results presented by Zhang et al. (2005) calculated at 1300 K and 25 GPa.

From the velocity distribution along different propagation directions (Figure S5 and S6), the v_P and v_S anisotropy, $A_{v_P}, A_{v_S}(\%) = 200\left(\frac{v_{max}-v_{min}}{v_{max}+v_{min}}\right)$ as well as the S-wave polarization anisotropy, $A_{v_{SP}}(\%) = \left(\frac{v_{S1}-v_{S2}}{v_{S1}+v_{S2}}\right)$, have been calculated using the Anis2k program (Mainprice, 1990) and plotted against pressure in Figure 5. Av_{SP} is roughly 1.5 times larger than Av_P,

moreover, both anisotropies smoothly decrease with increasing pressure from 32 to 26 % and from 19 to 13 %, respectively. At pressures of the akimotoite stability field, between approximately 21 and 24 GPa, however, the degree of anisotropy is still significant and greater than any other transition zone mineral, implying that akimotoite could still be the source of anisotropy in the lower transition zone noted in some seismic studies. The Av_P and Av_{SP} anisotropies at room pressure calculated from the elastic tensor by Weidner and Ito (1985) are slightly larger (21 and 35 %) than the anisotropies determined in this study (19 and 32 %). The computational study by Zhang et al. (2005) reports a Av_{SP} ~2 % larger at room pressure (green lines in Figure 5) but with a more pronounced decrease with pressure, whereas Av_P which is 3 % smaller, decreases with pressure, but above 15 GPa starts to increase again. Da Silva et al. (1999) (purple lines in Figure 5) report smaller Av_P and Av_{SP} by ~3 and 5 %, respectively, however, their data show a similar behavior with pressure as reported in this study. Quite good agreement is found with the computational study of Hao et al. (2019) (pink in Figure 5). Both Av_P and Av_{SP} of Hao et al. (2019) calculated at 300 K are less than 1.5 % different from those obtained in this study and have a similar trend as a function of pressure. The high temperature computations of Zhang et al. (2005) and Hao et al. (2019) indicate an increase in Av_P and Av_{SP} at room pressure.

Insert Figure 5

By a pressure of 21-24 GPa, however, where akimotoite is stable, the results of Hao et al. (2019) indicate that Av_P is essentially independent of temperature, at least up to 2000 K at 25 GPa, whereas at the same pressures Av_{SP} decreases by ~5 % at 2000 K (from ~25 % to ~20 %). Given the relatively small predicted effect of temperature, akimotoite will remain the mineral with the potential to display the highest seismic anisotropy near the base of the transition zone, as clearly visible in Figure 6, where a comparison is made with wadsleyite (Buchen et al., 2018), ringwoodite and Fe-bearing ringwoodite with 1.71 wt.% water (Schulze et al., 2018) and bridgmanite (Criniti et al., in revision).

Insert Figure 6

Deformation experiments on akimotoite have reported a temperature dependent fabric transition at approximately 1100 °C (Shiraishi et al., 2008). The CPO pattern reported at 1000 °C shows alignment of the *c*-axis perpendicular to the compression direction, whereas at 1300 °C it becomes subparallel (Shiraishi et al., 2008). This will give rise to a significant change in the P-wave velocity since its value is faster in the basal plane and much slower along the *c*-axis

(Figure S5, S6). The temperature-dependent CPO pattern of akimotoite may, therefore, be a plausible cause for the spatial variation of seismic anisotropy within the Tonga subducting slab (Shiraishi et al., 2008), for example, without the need of invoking other factors such as preferential orientation of inhomogeneities within the slab (Vavryčuk, 2006). On the other hand, it has been questioned whether the relatively low strains expected in the interiors of subducting slabs would be sufficient to produce suitably strong CPO in akimotoite-bearing rocks to cause detectible seismic anisotropy (Faccenda et al., 2014).

4 Conclusions

1) For the first time, the equation of state of the $MgSiO_3$ akimotoite end-member has been determined using a high-quality single-crystal of akimotoite up to pressures compatible with the base of the transition zone, i.e. to the pressure of the akimotoite stability. Both bulk and axial compressibility have been investigated and compared to literature data. The refined isothermal bulk modulus, K_T, of 205(1) GPa is smaller than those determined in compression studies on polycrystalline samples. The anisotropy in axial compressibility of akimotoite decreases slightly with pressure, in agreement with the elastic anisotropy.

2) The full elastic tensor of $MgSiO_3$ akimotoite has been experimentally determined using a combination of Brillouin spectroscopy and single-crystal X-ray diffraction in a diamond anvil cell up to 25 GPa. The room pressure data are in good agreement with the results presented by Weidner and Ito (1985). Compressional and shear wave velocities were compared to literature data and were found to be slower than wave velocities determined using ultrasonic interferometry in the multi-anvil press, particularly in v_P. Compared to computational studies, the aggregate velocities were slightly faster (Da Silva et al., 1999) or slower (Hao et al., 2019) but still within the Reuss and Voigt bounds obtained in this study. The axial compressibilities calculated from s_{ij}'s from the Brillouin data are in excellent agreement with respect to X-ray diffraction data both determined in this study.

3) The determined stiffness coefficients allow the elastic anisotropy behavior of akimotoite to be calculated up to pressures of its stability field. Pressure decreases only slightly the elastic anisotropy, leaving $MgSiO_3$ akimotoite to be the most elastically anisotropic mineral in the transition zone. It may, therefore, may play a prominent role in causing seismic anisotropy in and around subducting slabs at the base of the transition zone.

Acknowledgments

The authors would like to thank Raphael Njul for polishing of the samples, Hans Keppler for his help with the FTIR, Sylvain Petitgirard, Dorothea Wiesner and Nobuyoshi Miyajima for their help cutting the single-crystals with the FIB and Detlef Krauße with his support with the EMPA. This work was supported by DFG grant FR1555/11. The FEI Scios DualBeam machine at the Bayerisches Geoinstitut (University of Bayreuth) was supported by German Science Foundation under grant INST 91/315-1 FUGG.

References

Angel, R.J., Finger, L.W., 2011. SINGLE: A program to control single-crystal diffractometers. J. Appl. Crystallogr. 44, 247–251. https://doi.org/10.1107/S0021889810042305

Angel, R.J., Gonzalez-platas, J., Alvaro, M., 2014. EosFit7c and a Fortran module (library) for equation of state calculations. Z. Kristallogr. 229, 405–419. https://doi.org/10.1515/zkri-2013-1711

Angel, R.J., Zhao, J., Bujak, M., 2005. Hydrostatic limits of pressure-transmitting media by single-crystal diffraction (abs), in: 2005 Salt Lake City Annual Meeting. Paper No. 155-7.

Ashida, T., Kume, S., Ito, E., Navrotsky, A., 1988. MgSiO3 ilmenite: Heat capacity, thermal expansivity, and enthalpy of transformation. Phys. Chem. Miner. 16, 239–245. https://doi.org/10.1007/BF00220691

Bolfan-Casanova, N., Keppler, H., Rubie, D.C., 2000. Water partitioning between nominally anhydrous minerals in the MgO-SiO2-H2O system up to 24 GPa: Implications for the distribution of water in the Earth's mantle. Earth Planet. Sci. Lett. 182, 209–221. https://doi.org/10.1016/S0012-821X(00)00244-2

Buchen, J., 2018. The Elastic Properties of Wadsleyite and Stishovite at High Pressures. PhD thesis, University of Bayreuth, pp. 199. https://doi.org/10.15495/EPub_UBT_00004410

Buchen, J., Marquardt, H., Speziale, S., Kawazoe, T., Boffa Ballaran, T., Kurnosov, A., 2018. High-pressure single-crystal elasticity of wadsleyite and the seismic signature of water in the shallow transition zone. Earth Planet. Sci. Lett. 498, 77–87. https://doi.org/10.1016/j.epsl.2018.06.027

Criniti, G., Kurnosov, A., Boffa Ballaran, T., Frost, D.J., Single-crystal elasticity of MgSiO3 bridgmanite to mid-lower mantle pressure. J. Geophys. Res. Solid Earth in revision.

Da Silva, C.R.S., Karki, B.B., Stixrude, L., Wentzcovitch, R.M., 1999. Ab initio study of the elastic behavior of MgSiO3 ilmenite at high pressure. Geophys. Res. Lett. 26, 943–946. https://doi.org/10.1029/1999GL900149

475 Dewaele, A., Loubeyre, P., Mezouar, M., 2004. Equations of state of six metals above 94
476 GPa. Phys. Rev. B - Condens. Matter Mater. Phys. 70, 1–8.
477 https://doi.org/10.1103/PhysRevB.70.094112

478 Dziewonski, A.M., Anderson, D.L., 1981. Preliminary reference Earth model. Phys. Earth
479 Planet. Inter. 25, 297–356. https://doi.org/10.1016/0031-9201(81)90046-7

480 Faccenda, M., Geoscienze, D., Padova, U., 2014. Mid mantle seismic anisotropy around
481 subduction zones. Phys. Earth Planet. Inter. 227, 1–19.
482 https://doi.org/10.1016/j.pepi.2013.11.015

483 Fukao, Y., Obayashi, M., 2013. Subducted slabs stagnant above, penetrating through, and
484 trapped below the 660 km discontinuity. J. Geophys. Res. Solid Earth 118, 5920–5938.
485 https://doi.org/10.1002/2013JB010466

486 Fukao, Y., Obayashi, M., Nakakuki, T., 2009. Stagnant Slab: A Review. Annu. Rev. Earth
487 Planet. Sci. 37, 19–46. https://doi.org/10.1146/annurev.earth.36.031207.124224

488 Fukao, Y., Widiyantoro, S., Obayashi, M., 2001. Stagnant slabs in the upper and lower mantle
489 transition region. Rev. Geophys. 39, 291–323. https://doi.org/10.1029/1999RG000068

490 Gasparik, T., 1990. Phase Relations in the Transition Zone. J. Geophys. Res. 95, 15,751-
491 15,769.

492 Hao, S., Wang, W., Qian, W., Wu, Z., 2019. Elasticity of akimotoite under the mantle
493 conditions: Implications for multiple discontinuities and seismic anisotropies at the depth
494 of ~600–750 km in subduction zones. Earth Planet. Sci. Lett. 528.
495 https://doi.org/10.1016/j.epsl.2019.115830

496 Hill, R., 1952. The elastic behaviour of a crystalline aggregate. Proc. Phys. Soc. A 65, 349–
497 354.

498 Hirose, K., 2002. Phase transitions in pyrolitic mantle around 670-km depth: Implications for
499 upwelling of plumes from the lower mantle. J. Geophys. Res. Solid Earth 107, ECV 3-1-
500 ECV 3-13. https://doi.org/10.1029/2001jb000597

501 Irifune, T., Higo, Y., Inoue, T., Kono, Y., Ohfuji, H., Funakoshi, K., 2008. Sound velocities
502 of majorite garnet and the composition of the mantle transition region. Nature 451, 814–

503 817. https://doi.org/10.1038/nature06551

504 Irifune, T., Ringwood, A.E., 1987. Phase transformations in a harzburgite composition to 26
505 GPa: implications for dynamical behaviour of the subducting slab. Earth Planet. Sci.
506 Lett. 86, 365–376. https://doi.org/10.1016/0012-821X(87)90233-0

507 Ishii, T., Kojitani, H., Akaogi, M., 2019. Phase Relations of Harzburgite and MORB up to the
508 Uppermost Lower Mantle Conditions: Precise Comparison With Pyrolite by
509 Multisample Cell High-Pressure Experiments With Implication to Dynamics of
510 Subducted Slabs. J. Geophys. Res. Solid Earth 124, 3491–3507.
511 https://doi.org/10.1029/2018JB016749

512 Ishii, T., Kojitani, H., Akaogi, M., 2011. Post-spinel transitions in pyrolite and Mg2SiO4 and
513 akimotoite-perovskite transition in MgSiO3: Precise comparison by high-pressure high-
514 temperature experiments with multi-sample cell technique. Earth Planet. Sci. Lett. 309,
515 185–197. https://doi.org/10.1016/j.epsl.2011.06.023

516 Kantor, I., Prakapenka, V., Kantor, A., Dera, P., Kurnosov, A., Sinogeikin, S., Dubrovinskaia,
517 N., Dubrovinsky, L., 2012. BX90: A new diamond anvil cell design for X-ray diffraction
518 and optical measurements. Rev. Sci. Instrum. 83. https://doi.org/10.1063/1.4768541

519 Kato, T., 1986. Stability relation of (Mg,Fe)SiO3 garnets, major constituents in the Earth's
520 interior. Earth Planet. Sci. Lett. 77, 399–408. https://doi.org/10.1016/0012-
521 821X(86)90149-4

522 Kennett, B.L.N., Engdah, E.R., Buland, R., 1995. Constraints on seismic velocities in the
523 Earth from traveltimes. Geophys. J. Int. 122, 108–124.

524 King, H.E., Finger, L.W., 1979. Diffracted beam crystal centering and its application to high-
525 pressure crystallography. J. Appl. Crystallogr. 12, 374–378.
526 https://doi.org/10.1107/s0021889879012723

527 Kurnosov, A., Kantor, I., Boffa-Ballaran, T., Lindhardt, S., Dubrovinsky, L., Kuznetsov, A.,
528 Zehnder, B.H., 2008. A novel gas-loading system for mechanically closing of various
529 types of diamond anvil cells. Rev. Sci. Instrum. 79. https://doi.org/10.1063/1.2902506

530 Mainprice, D., 2015. Seismic Anisotropy of the Deep Earth from a Mineral and Rock Physics
531 Perspective, Treatise on Geophysics: Second Edition. Elsevier B.V.

https://doi.org/10.1016/B978-0-444-53802-4.00044-0

Mainprice, D., 1990. A Fortran program to calculate seismic anisotropy from the lattice preferred orientation of minerals. Comput. Geosci. 16, 385–393.

Montagner, J.P., Kennett, B.L.N., 1996. How to reconcile body-wave and normal-mode reference earth models. Geophys. J. Int. 125, 229–248. https://doi.org/10.1111/j.1365-246X.1996.tb06548.x

Nowacki, A., Kendall, J.-M., Wookey, J., Pemberton, A., 2015. Mid-mantle anisotropy in subduction zones and deep water transport. Geochemistry Geophys. Geosystems 16, 764–784.

Nye, J.F., 1985. Physical properties of crystals: their representation by tensors and matrices. Oxford Science Publications, 322 pp.

Ohtani, E., Kagawa, N., Fujino, K., 1991. Stability of majorite (Mg, Fe)SiO3 at high pressures and 1800°C. Earth Planet. Sci. Lett. 102, 158–166. https://doi.org/10.1016/0012-821X(91)90005-3

Pamato, M.G., Kurnosov, A., Boffa Ballaran, T., Frost, D.J., Ziberna, L., Giannini, M., Speziale, S., Tkachev, S.N., Zhuravlev, K.K., Prakapenka, V.B., 2016. Single crystal elasticity of majoritic garnets: Stagnant slabs and thermal anomalies at the base of the transition zone. Earth Planet. Sci. Lett. 451, 114–124. https://doi.org/10.1016/j.epsl.2016.07.019

Paterson, M.S., 1982. The determination of hydroxyl by infrared adsorption in quartz, silicate glasses and similar materials. Bull. Mineral. 105, 20–29. https://doi.org/10.3406/bulmi.1982.7582

Reynard, B., Fiquet, G., Itié, J.P., Rubie, D.C., 1996. High-pressure X-ray diffraction study and equation of state of MgSiO3 ilmenite. Am. Mineral. 81, 45–50. https://doi.org/10.2138/am-1996-1-206

Sawamoto, H., 1987. Phase Diagram of MgSiO3 at Pressures up to 24 GPa and Temperatures up to 2200 °C: Phase Stability and Properties of Tetragonal Garnet, in: High-Pressure Research in Mineral Physics. American Geophysical Union, Washington, D.C., pp. 209–219.

561 Schulze, K., Marquardt, H., Kawazoe, T., Boffa Ballaran, T., McCammon, C., Koch-Müller,
562 M., Kurnosov, A., Marquardt, K., 2018. Seismically invisible water in Earth's transition
563 zone? Earth Planet. Sci. Lett. 498, 9–16. https://doi.org/10.1016/j.epsl.2018.06.021

564 Shatskiy, A., Fukui, H., Matsuzaki, T., Shinoda, K., Yoneda, A., Yamazaki, D., Ito, E.,
565 Katsura, T., 2007. Growth of large (1 mm) MgSiO3 perovskite single crystals: A thermal
566 gradient method at ultrahigh pressure. Am. Mineral. 92, 1744–1749.
567 https://doi.org/10.2138/am.2007.2415

568 Shiraishi, R., Ohtani, E., Kanagawa, K., Shimojuku, A., Zhao, D., 2008. Crystallographic
569 preferred orientation of akimotoite and seismic anisotropy of Tonga slab. Nature 455,
570 657–660. https://doi.org/10.1038/nature07301

571 Stixrude, L., Lithgow-Bertelloni, C., 2005. Thermodynamics of mantle minerals - I. Physical
572 properties. Geophys. J. Int. 162, 610–632. https://doi.org/10.1111/j.1365-
573 246X.2005.02642.x

574 Trampert, J., Van Heijst, H.J., 2002. Global azimuthal anisotropy in the transition zone.
575 Science (80-.). 296, 1297–1299. https://doi.org/10.1126/science.1070264

576 Trots, D.M., Kurnosov, A., Ballaran, T.B., Tkachev, S., Zhuravlev, K., Prakapenka, V.,
577 Berkowski, M., Frost, D.J., 2013. The Sm:YAG primary fluorescence pressure scale. J.
578 Geophys. Res. Solid Earth 118, 5805–5813. https://doi.org/10.1002/2013JB010519

579 Trots, D.M., Kurnosov, A., Vasylechko, L., Berkowski, M., Ballaran, T.B., Frost, D.J., 2011.
580 Elasticity and equation of state of Li2B4O7. Phys. Chem. Miner. 38, 561–567.
581 https://doi.org/10.1007/s00269-011-0428-1

582 Van Der Hilst, R., Engdahl, R., Spakman, W., Nolet, G., 1991. Tomographic imaging of
583 subducted lithosphere below northwest Pacific island arcs. Nature 353, 37–43.
584 https://doi.org/10.1038/353037a0

585 Vavryčuk, V., 2006. Spatially dependent seismic anisotropy in the Tonga subduction zone: A
586 possible contributor to the complexity of deep earthquakes. Phys. Earth Planet. Inter.
587 155, 63–72. https://doi.org/10.1016/j.pepi.2005.10.005

588 Wang, Y., Uchida, T., Zhang, J., Rivers, M.L., Sutton, S.R., 2004. Thermal equation of state
589 of akimotoite MgSiO3 and effects of the akimotoite-garnet transformation on

seismicstructure near the 660 km discontinuity. Phys. Earth Planet. Inter. 143, 57–80. https://doi.org/10.1016/j.pepi.2003.08.007

Watt, J.P., Davies, G.F., O'Connell, R.J., 1976. The elastic properties of composite materials. Rev. Geophys. 14, 541–563. https://doi.org/10.1029/RG014i004p00541

Weidner, D.J., Ito, E., 1985. Elasticity of MgSiO3 in the ilmenite phase. Phys. Earth Planet. Inter. 40, 65–70. https://doi.org/10.1016/0031-9201(85)90006-8

Yuan, K., Beghein, C., 2013. Seismic anisotropy changes across upper mantle phase transitions. Earth Planet. Sci. Lett. 374, 132–144. https://doi.org/10.1016/j.epsl.2013.05.031

Zhang, Y., Wang, Y., Wu, Y., Bina, C.R., Jin, Z., Dong, S., 2013. Phase transitions of harzburgite and buckled slab under eastern China. Geochemistry, Geophys. Geosystems 14, 1182–1199. https://doi.org/10.1002/ggge.20069

Zhang, Y., Zhao, D., Matsui, M., 2005. Anisotropy of akimotoite: A molecular dynamics study. Phys. Earth Planet. Inter. 151, 309–319. https://doi.org/10.1016/j.pepi.2005.04.003

Zhou, C., Gréaux, S., Nishiyama, N., Irifune, T., Higo, Y., 2014. Sound velocities measurement on MgSiO 3 akimotoite at high pressures and high temperatures with simultaneous in situ X-ray diffraction and ultrasonic study. Phys. Earth Planet. Inter. 228, 97–105. https://doi.org/10.1016/j.pepi.2013.06.005

Tables

Table 1. Elastic moduli obtained in this study from X-ray diffraction (XRD) and Brillouin spectroscopy (BS). For comparison, the parameters determined using XRD by Weidner and Ito (1985), Reynard et al. (1996), Wang et al. (2004) and Zhou et al. (2014) as well as the refitted parameters using a BM3 EoS are listed. Furthermore, the elastic moduli determined from three computational studies (Da Silva et al., 1999; Zhang et al., 2005; Hao et al., 2019) are reported.

	V_0 (Å^3)	K_{T0} (GPa)	K_{S0} (GPa)	K'	G_0 (GPa)	G'
This study - XRD	262.43(2)	205(1)	207[a]	4.9(2)		
This study – BS			209(2)	4.4(1)	131(1)	1.7(1)
Weidner and Ito (1985)	263.56		212	-	132	-
Reynard et al. (1996)	262.17(49)	212[b]		5.6(10)		
Reynard et al. (1996) refitted	262.0(3)	228(8)		4		
Wang et al. (2004)	263.9(2)	210[b]		5.6(8)		
Wang et al. (2004) refitted	264.4(9)	212(15)		4		
Zhou et al. (2014)	262.53(5)		219.4(7)	4.62(3)	132.1(7)	1.63(4)
Da Silva et al. (1999)[c]		222		4.5	144	1.6
Zhang et al. (2005)		221	226	3.85	136	1.04
Hao et al. (2019) - EoS	261.83	211		4.37		
Hao et al. (2019) – DFT			202		126	

Note: the refitted parameters have been obtained from the reported *P*-*V* data using the EoSFit program

[a] value recalculated using $K_{S0} = K_{T0} * (1 + \alpha\gamma T)$ with α = 2.44x10^{-5} 1/K (Ashida et al., 1988), γ = 1.18 (Stixrude & Lithgow-Bertelloni, 2005), T = 298 K

[b] Reynard et al. (1996) and Wang et al. (2004) fixed the value of K_{T0} using the value of K_{S0} from Weidner and Ito (1985)

[c] Data from Da Silva et al. (1999) are at 0 K and 0 GPa

Table 2. Unit-cell lattice parameters of crystals X1 and X2 measured in the two DAC experiments up to 24.9(1) GPa. The pressure reported was calculated using the ruby fluorescence lines following Dewaele et al. (2004).

	X1			X2		
P_{ruby} (GPa)	*a* (Å)	*c* (Å)	*V* (Å^3)	*a* (Å)	*c* (Å)	*V* (Å^3)
DAC1						
0.0001(1)	4.7275(5)	13.5578(12)	262.41(6)	4.7274(3)	13.5577(2)	262.40(3)
0.60(5)	4.7238(3)	13.5391(8)	261.64(4)	4.7236(3)	13.5414(2)	261.66(3)
1.10(1)	4.7210(4)	13.5257(10)	261.07(4)	4.7206(3)	13.5274(2)	261.06(3)
2.07(11)	4.7142(2)	13.4981(5)	259.79(2)	4.7142(3)	13.4998(3)	259.82(3)
3.93(1)	4.7031(2)	13.4488(4)	257.62(2)	4.7032(3)	13.4507(2)	257.67(3)
4.07(1)	4.7030(3)	13.4476(6)	257.59(3)	4.7030(3)	13.4489(2)	257.61(3)
6.20(6)	4.6899(3)	13.3900(7)	255.06(3)	4.6897(6)	13.3928(6)	255.09(6)
6.48(6)	4.6880(3)	13.3835(6)	254.73(3)	4.6878(2)	13.3850(3)	254.74(3)
7.88(3)	4.6805(2)	13.3509(4)	253.30(2)	4.6800(3)	13.3528(3)	253.27(3)
8.00(20)	4.6803(2)	13.3498(5)	253.25(2)	4.6798(3)	13.3513(4)	253.23(3)
9.45(14)	4.6726(3)	13.3141(8)	251.75(3)	4.6722(3)	13.3169(4)	251.75(3)
10.68(3)	4.6657(4)	13.2826(11)	250.40(5)	4.6649(3)	13.2890(4)	250.44(3)
12.14(6)	4.6582(5)	13.2500(11)	248.99(5)	4.6579(6)	13.2518(8)	248.99(6)
DAC2						
0.0001(1)	4.7279(5)	13.5534(14)	262.37(5)	4.7275(4)	13.5582(4)	262.42(5)
0.23(3)	4.7266(4)	13.5470(12)	262.10(5)	4.7263(2)	13.5513(2)	262.15(2)
7.37(3)	4.6849(7)	13.3674(20)	254.09(7)	4.6849(9)	13.3702(10)	254.14(10)
13.88(5)	4.6520(11)	13.2090(31)	247.56(11)	4.6487(14)	13.2234(12)	247.48(15)
14.07(38)	4.6507(14)	13.2007(40)	247.27(14)	4.6466(10)	13.2157(9)	247.11(11)
16.37(1)	4.6379(11)	13.1610(32)	245.17(11)	4.6361(11)	13.1714(9)	245.17(11)
16.37(1)	4.6394(12)	13.1696(38)	245.48(11)	4.6387(8)	13.1657(10)	245.34(8)
17.40(2)	4.6358(15)	13.1495(43)	244.73(15)	4.6351(10)	13.1516(14)	244.69(10)
17.72(10)	4.6340(10)	13.1486(10)	244.53(11)	4.6340(10)	13.1486(10)	244.53(11)
17.44(9)	4.6327(6)	13.1481(16)	244.37(5)	4.6328(7)	13.1508(9)	244.44(8)
19.91(21)	4.6205(5)	13.0986(13)	242.18(5)	4.6213(8)	13.1035(9)	242.36(9)
22.05(12)	4.6115(5)	13.0617(14)	240.55(5)	4.6111(4)	13.0658(5)	240.59(4)
24.86(3)	4.5996(7)	13.0143(19)	238.44(7)	4.5986(6)	13.0162(7)	238.38(7)
7.79(28)	4.6796(4)	13.3505(13)	253.19(4)	4.6788(9)	13.3523(10)	253.13(9)

Table 3. Single-crystal stiffness coefficients c_{ij}'s, absolute pressure (P_{abs}), pressure calculated using the ruby calibration reported by Dewaele et al. (2004) and density measured by single-crystal X-ray diffraction. The RVH average bulk (isothermal K_T and adiabatic K_S) and shear moduli are reported, as well as the aggregate velocities v_P and v_S. K_T was calculated using the relation: $\boldsymbol{K_S = K_T * (1 + \alpha\gamma T)}$ with α = 2.44x10^{-5} 1/K (Ashida et al., 1988), γ = 1.18 (Stixrude and Lithgow-Bertelloni, 2005) and T = 298 K.

P_{abs} (GPa)	P_{ruby} (GPa)	density (g/cm^3)	c_{11} (GPa)	c_{33} (GPa)	c_{44} (GPa)	c_{12} (GPa)	c_{13} (GPa)	c_{14} (GPa)	c_{25} (GPa)	K_T (GPa)	K_S (GPa)	G (GPa)	v_P (km/s)	v_S (km/s)
0.00	0.0001(1)	3.8117(5)	457(2)	368(2)	104(1)	153(3)	78(2)	23(1)	-21(2)	206(1)	208(1)	130(1)	10.01(2)	5.84(1)
3.95	3.93(1)	3.8822(2)	482(2)	390(4)	115(1)	171(3)	99(2)	12(1)	-32(1)	227(1)	229(1)	137(1)	10.30(2)	5.93(2)
8.04	7.79(3)	3.9509(8)	495(2)	410(2)	121(1)	172(3)	106(2)	13(1)	-32(1)	236(2)	238(1)	144(1)	10.44(2)	6.03(1)
10.74	10.68(3)	3.9941(8)	531(2)	430(2)	128(1)	198(3)	120(1)	11(1)	-32(1)	258(1)	260(1)	149(1)	10.72(2)	6.11(1)
12.22	12.14(6)	4.0171(5)	528(2)	435(2)	131(1)	190(3)	124(1)	12(1)	-36(1)	258(1)	260(1)	150(1)	10.71(1)	6.12(1)
14.14	14.07(38)	4.0464(7)	543(2)	447(2)	135(1)	198(3)	129(2)	15(1)	-35(1)	267(1)	269(1)	154(1)	10.84(1)	6.17(1)
16.10	16.37(1)	4.0757(14)	555(2)	463(2)	140(1)	206(3)	141(2)	14(1)	-36(1)	278(1)	281(1)	158(1)	10.98(2)	6.22(1)
17.25	17.44(10)	4.0925(11)	565(4)	459(6)	143(2)	210(6)	155(4)	15(2)	-37(2)	287(3)	289(3)	158(1)	11.06(4)	6.22(3)
19.76	19.91(21)	4.1286(8)	579(2)	477(3)	147(1)	224(3)	151(2)	13(1)	-37(1)	293(1)	296(1)	163(1)	11.14(2)	6.28(1)
21.84	22.05(12)	4.1577(8)	576(2)	486(2)	150(1)	217(3)	162(2)	14(1)	-38(1)	298(1)	300(1)	164(1)	11.17(1)	6.28(1)
24.61	24.86(3)	4.1954(5)	595(2)	502(2)	155(1)	233(3)	170(2)	11(1)	-39(1)	310(1)	313(1)	168(1)	11.31(1)	6.32(1)

Note $c_{66} = 0.5\ (c_{11} - c_{12})$

Figures

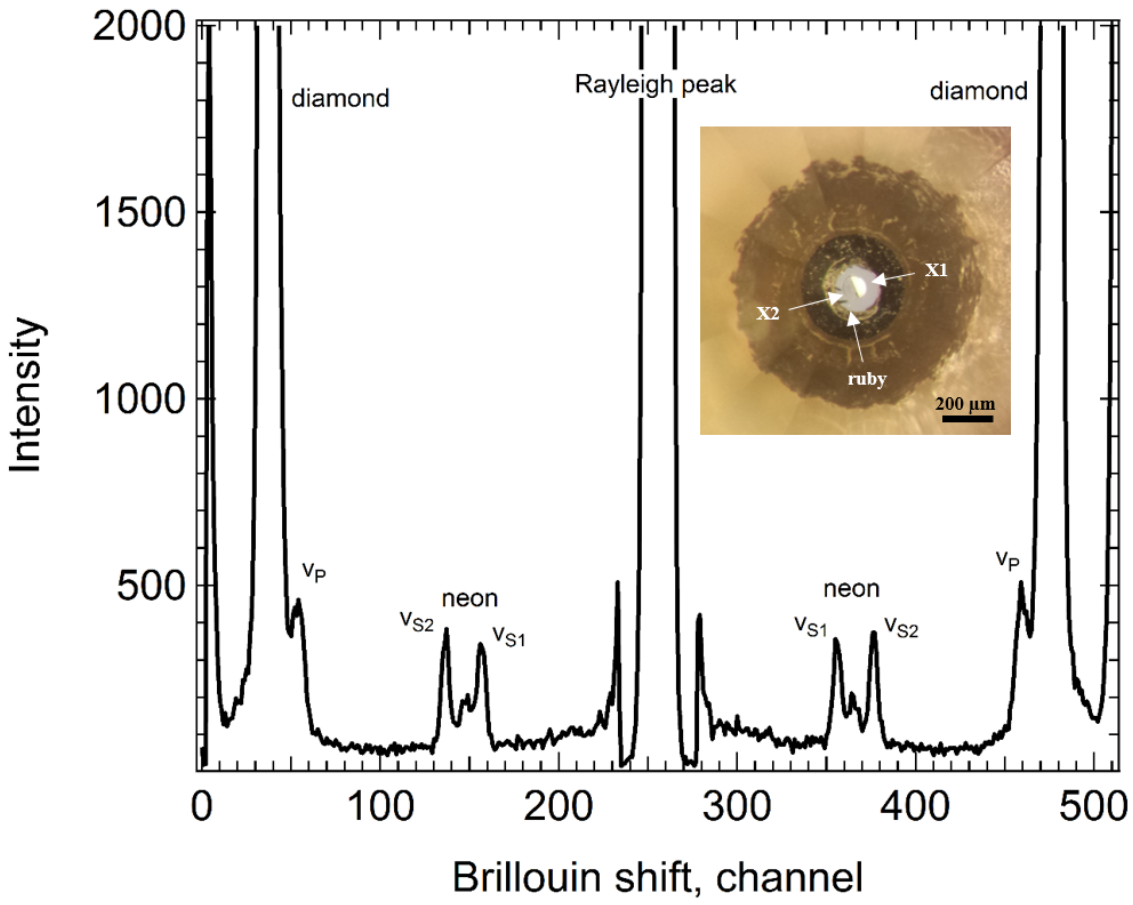

Figure 1. Representative Brillouin spectrum collected for the X2 single-crystal at 4 GPa. The Rayleigh peak corresponding to the elastic scattering can be seen at the center, whereas two broad and intense signals due to the diamond anvils can be seen at the border of the Brillouin spectrum. Three signals from akimotoite, v_P, v_{S1} and v_{S2} are visible. A signal due to the Ne pressure medium is visible between the v_{S1} and v_{S2} signals. All peaks shift to higher velocities with increasing pressure. The inset shows an optical image of a loaded diamond anvil cell sample chamber at a pressure of 3.93(1) GPa. The two half-circles X1 and X2 have different orientations as shown by the different extinction colors. The small ruby sphere used for in-situ pressure determination is visible close to the gasket.

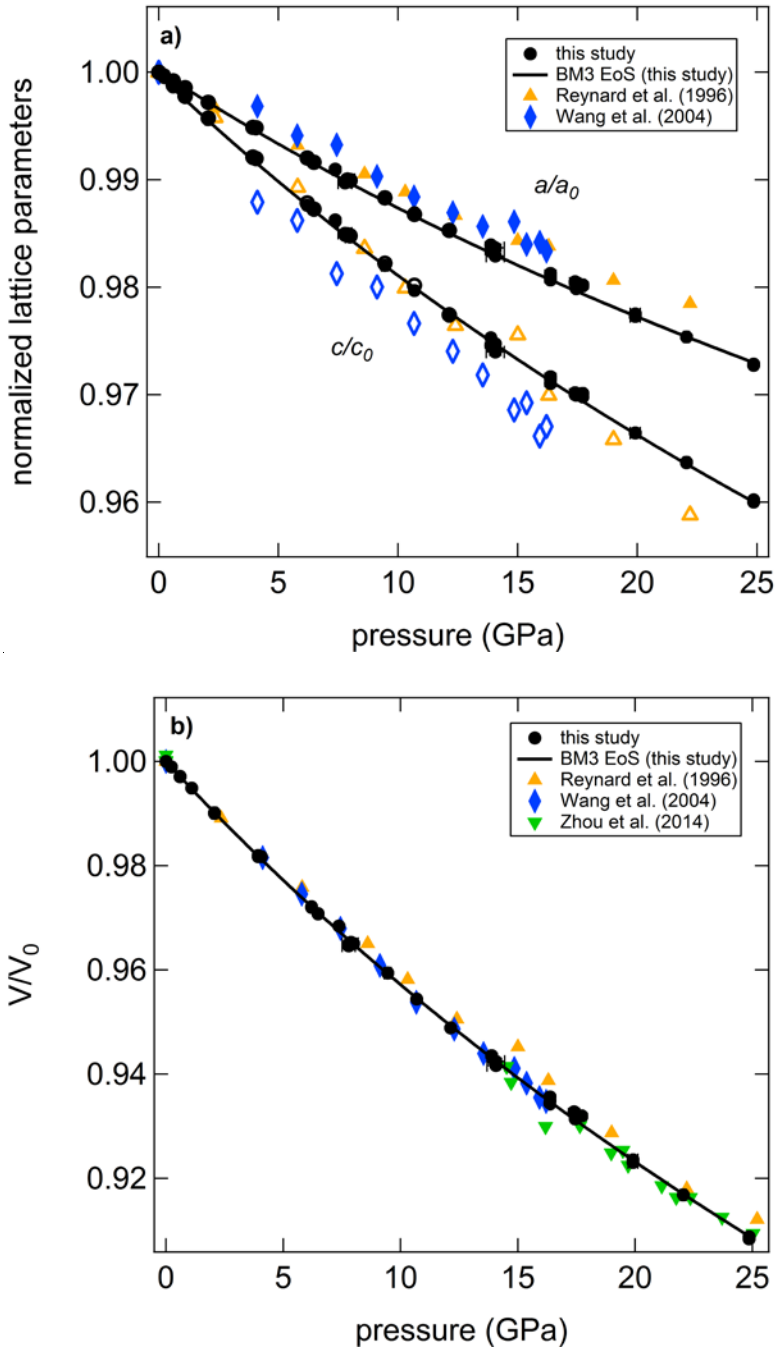

Figure 2. Variation with pressure of the unit-cell lattice parameters normalized with respect to the room pressure values. (a) a/a_0 and c/c_0 and (b) unit-cell volumes. The solid lines represent BM3 EoS fits to the data obtained in this study. The normalized volumes from Wang et al. (2004) (blue diamonds) and Zhou et al. (2014) (green triangles) are in agreement with this study, especially at pressures below 15 GPa, however the axial anisotropy reported by Wang et al. (2004) is more accentuated than that measured in this study. The volume data reported by Reynard et al. (1996) are stiffer than those obtained in this study likely due to their stiffer *a*-axis.

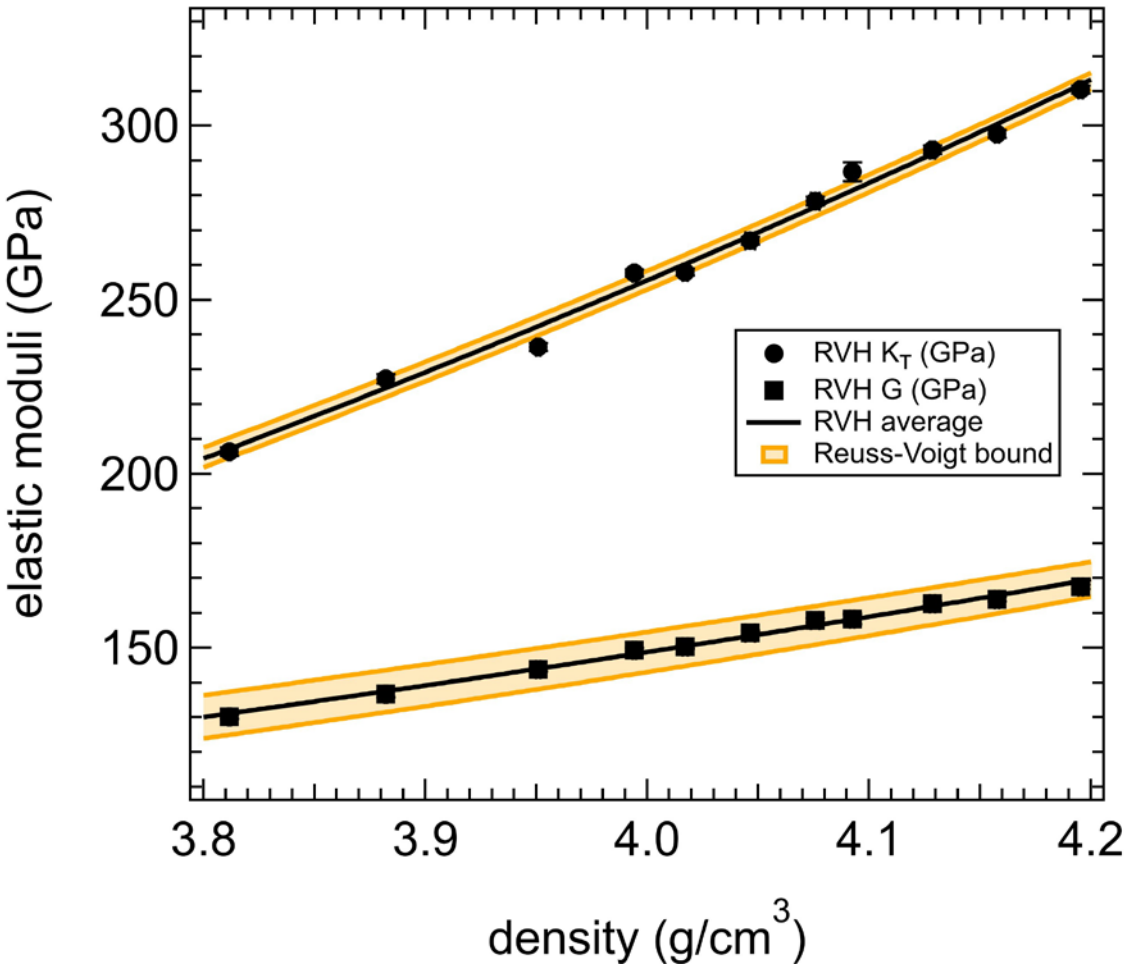

Figure 3. Elastic moduli K_T and G versus density. The black circles represent the aggregate isothermal bulk and shear moduli of akimotoite calculated according to the Reuss-Voigt-Hill (RVH) average of the Voigt and Reuss bounds determined from the experimental elastic stiffness and compliance coefficients. The solid lines represent BM3 EoS fits through the RVH average. The shaded orange areas represent the Reuss-Voigt bounds. The uncertainties are smaller than the symbol size.

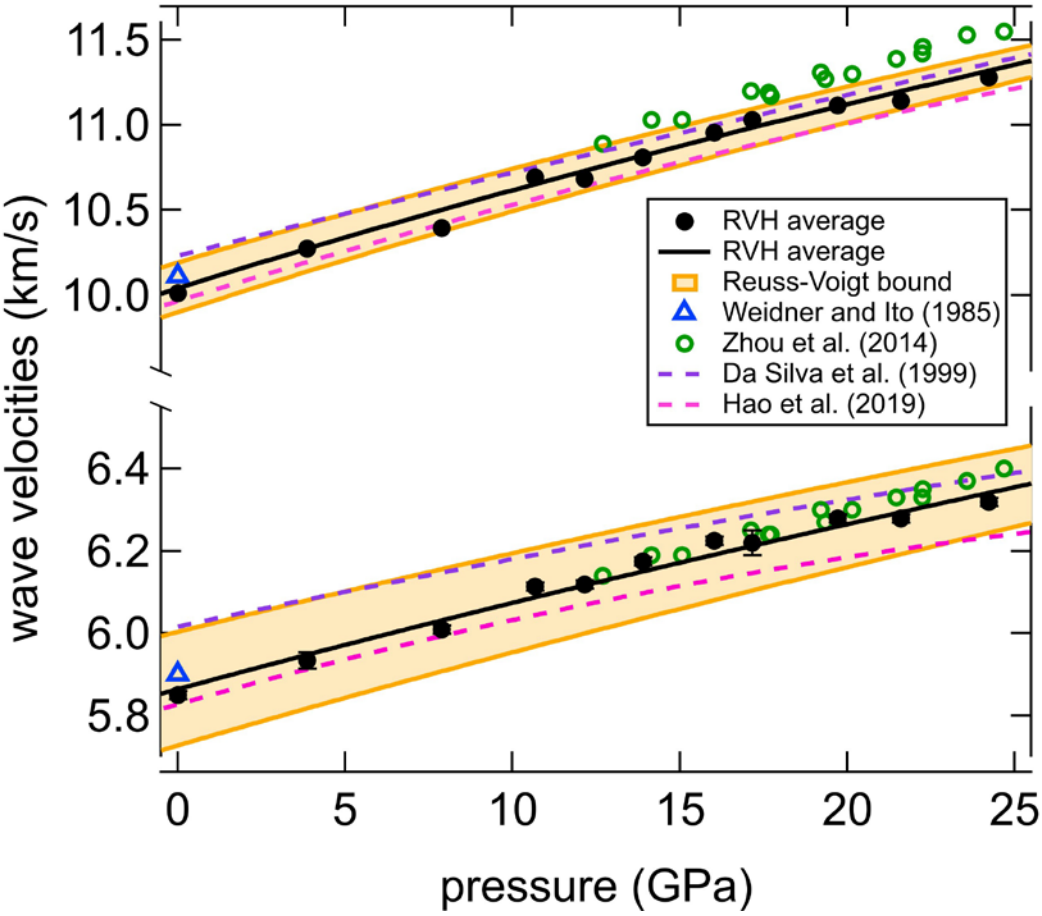

669
670

671 **Figure 4.** Variation with pressure of the aggregate longitudinal and shear wave velocities of
672 $MgSiO_3$ akimotoite. The shaded orange areas represent the Reuss-Voigt bounds. The
673 uncertainties are smaller than the symbol size. For comparison, the aggregate velocities reported
674 by Weidner and Ito (1985) at room pressure and by Zhou et al. (2014) at high-pressures, as well
675 as the results from two computational studies (Da Silva et al., 1999; Hao et al., 2019) are
676 reported.

677

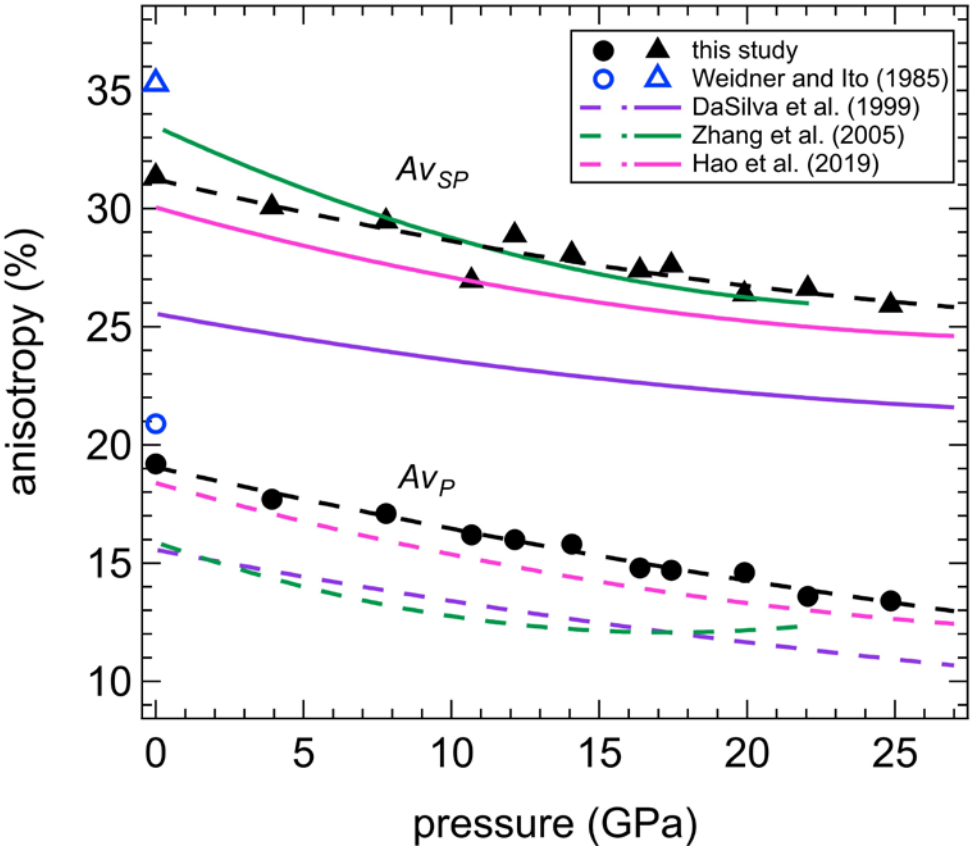

678

679

680 **Figure 5.** P-wave anisotropy (Av_P) and S-wave polarization anisotropy (Av_{SP}) of $MgSiO_3$
681 akimotoite with increasing pressure. The uncertainties are smaller than the symbol size. For
682 comparison, the anisotropies calculated using the elastic tensor at room pressure by Weidner
683 and Ito (1985) and those from three computational studies (Da Silva et al., 1999; Zhang et al.,
684 2005; Hao et al., 2019) also are reported.

685

686

687

688

689

690

691

692

693

694

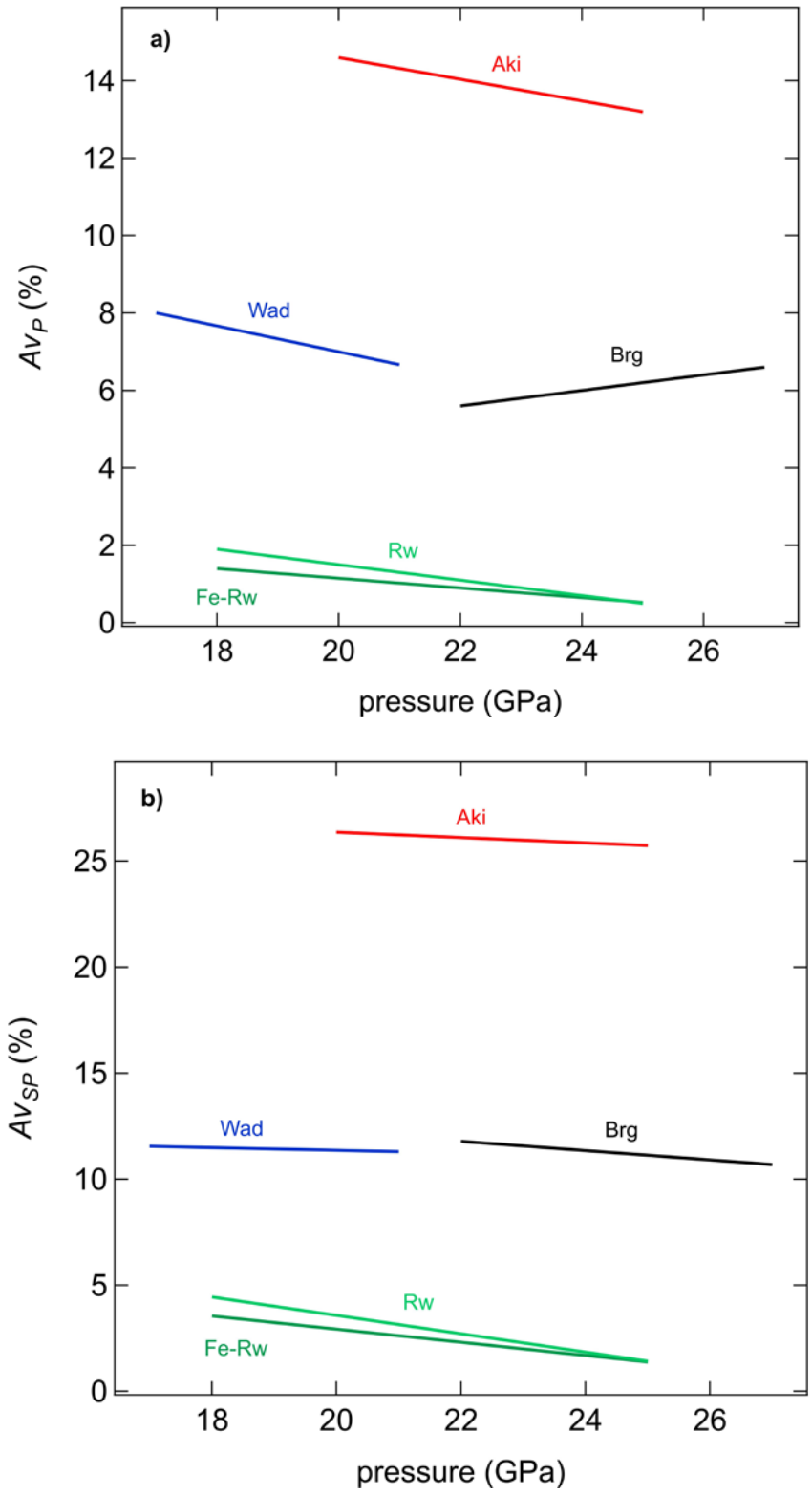

Figure 6. a) P-wave anisotropy (Av_P) and b) S-wave polarisation anisotropy (Av_{SP}) calculated for different minerals at pressures of the Earth's transition zone; Akimotoite (Aki, this study), wadsleyite (Wad) (Buchen et al., 2018), ringwoodite and Fe-bearing ringwoodite (Fe-Rw) with 1.71 wt% water (Schulze et al., 2018) and bridgmanite (Brg) (Criniti et al., in revision).

Supplementary material

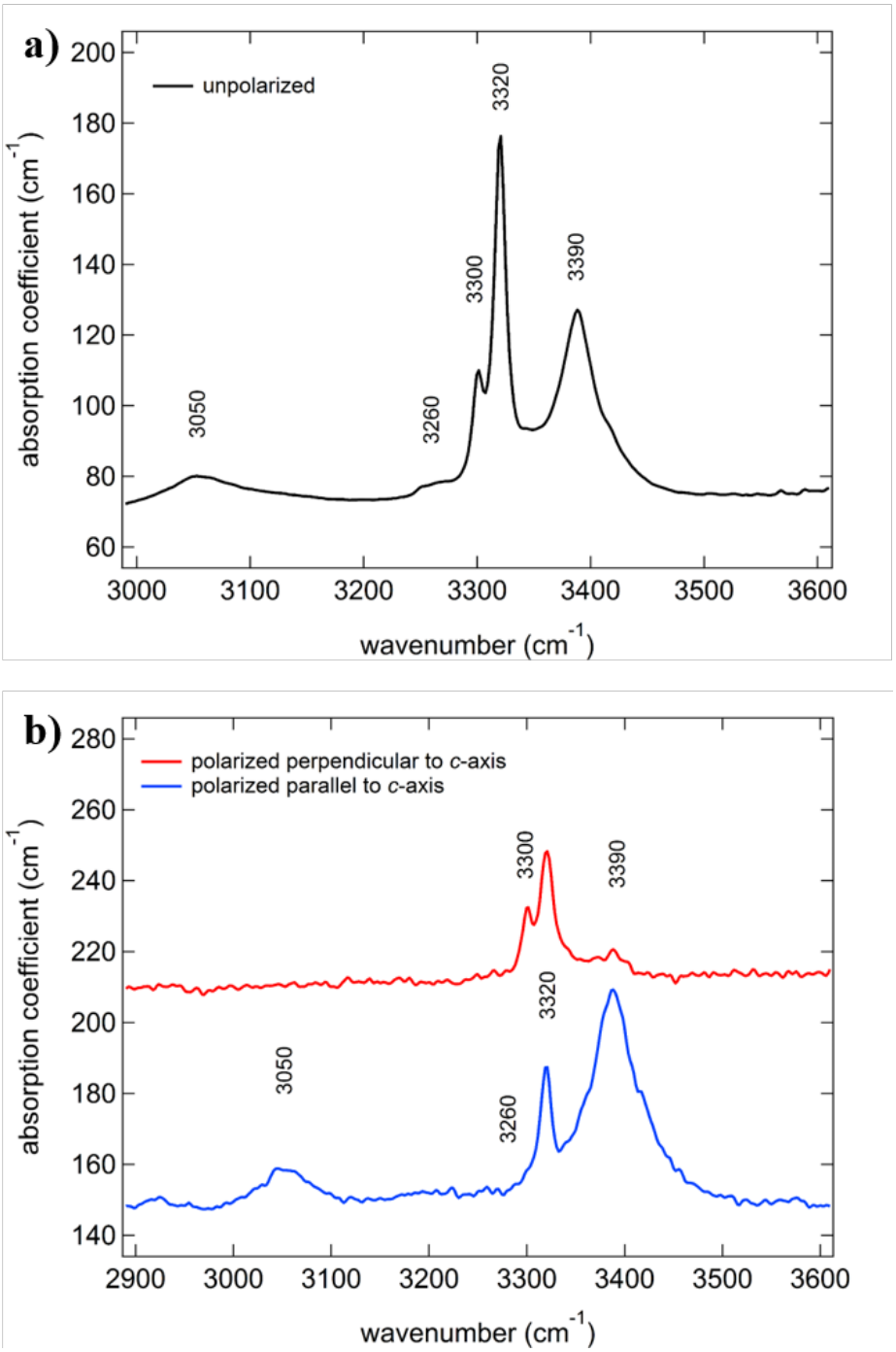

Figure S1. a) Unpolarized and b) polarized FTIR spectra of akimotoite perpendicular (red) and parallel (blue) to the *c*-axis collected on a crystal that was oriented parallel to the (100) plane. Fitting of these FTIR spectra yielded a H_2O content of ~ 280 ppm.

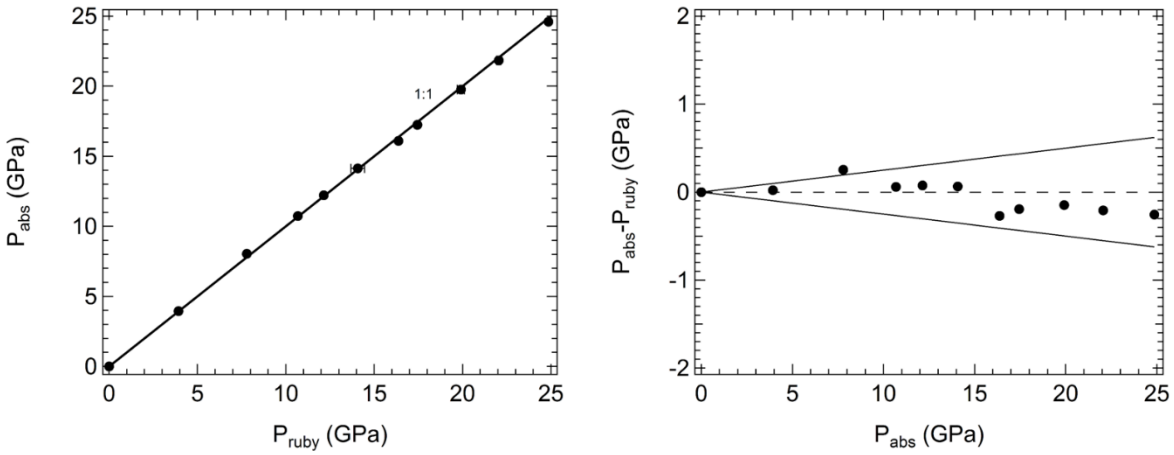

Figure S2. Comparison of the absolute pressure with the pressure calculated using the ruby fluorescence calibration reported by Dewaele et al. (2004). The solid lines in the plot on the right represent the uncertainty (2.5 %) of the ruby pressure scale.

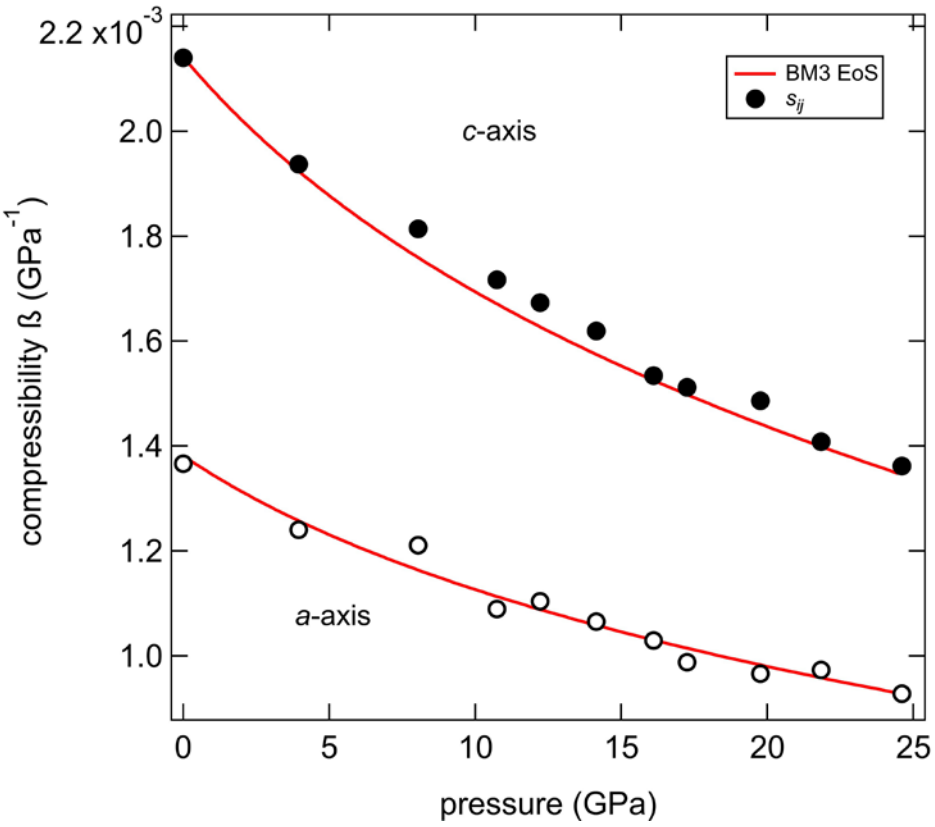

721

722

723 **Figure S3.** Change in compressibility *ß* of the *a*- and *c*-axes with increasing pressure
724 determined from X-ray diffraction (red) and the compliance tensor s_{ij} obtained with Brillouin
725 spectroscopy (black). Results from both methods are in very good agreement with one another
726 for the stiffer *a*-axis, however, for the *c*-axis the X-ray data suggest a slightly more compressible
727 behavior than the Brillouin data.

728

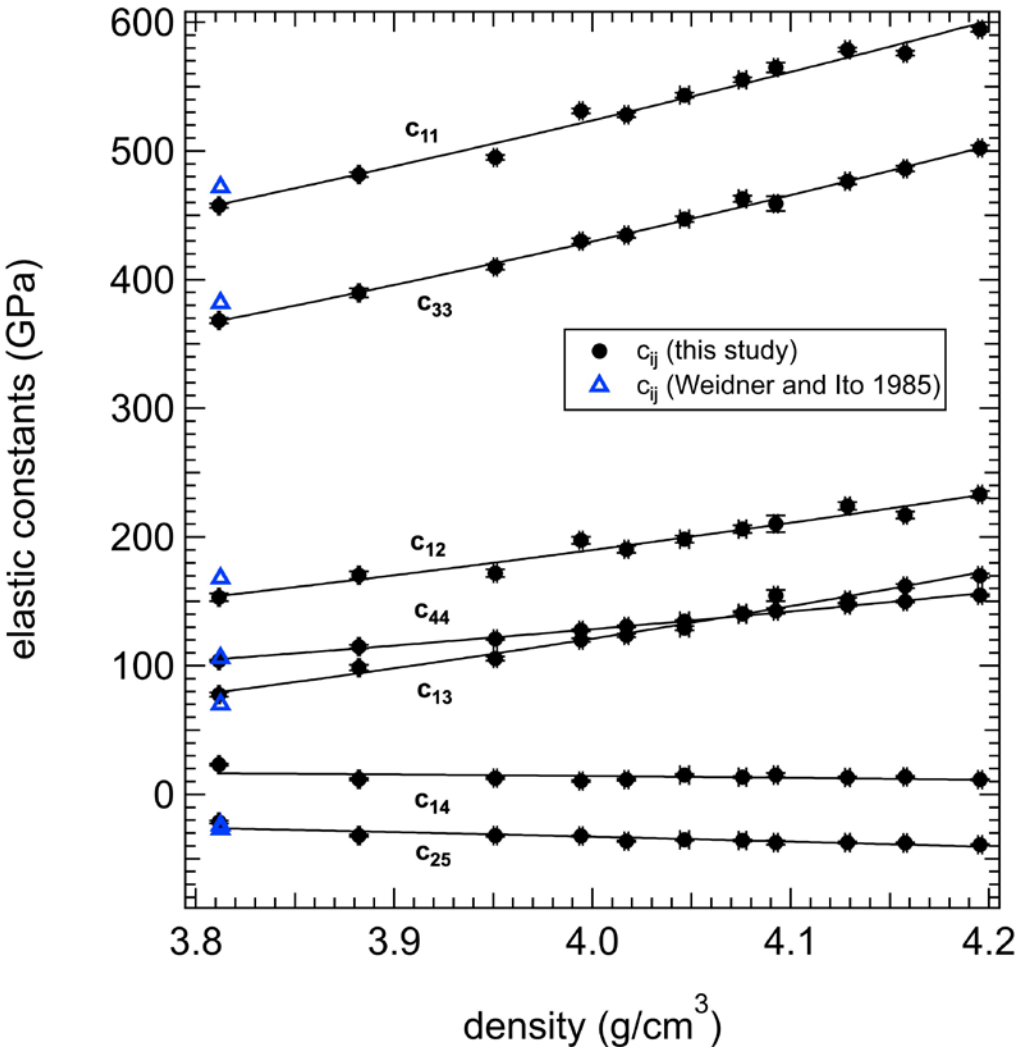

Figure S4. Variation with pressure of the stiffness coefficients c_{ij} of akimotoite. For comparison the data at room pressure from Weidner and Ito (1985) also are reported. The black solid lines represent third-order finite strain expressions of the individual elastic moduli following Stixrude and Lithgow-Bertelloni (2005):

$$c_{ijkl} = (1+2f)^{5/2}\left\{c_{ijkl0} + \left(3K_0 c'_{ijkl0} - 5c_{ijkl0}\right)f + \left[6K_0 c'_{ijkl0} - 14c_{ijkl0} - \frac{3}{2}K_0\delta_{kl}^{ij}(3K'_0 - 16)\right]f^2\right\}$$

with $f = \frac{1}{2}\left[\left(\frac{\rho}{\rho_0}\right)^{2/3} - 1\right]$ and $\delta_{kl}^{ij} = -\delta_{ij}\delta_{kl} - \delta_{il}\delta_{jk} - \delta_{jl}\delta_{ik}$ where δ_{ij} is the Kronecker delta. ρ_0, K_0 and K_0' were fixed to the values reported in Table 1 and 3. The resulting parameters for c_{ij} and c_{ij}' are reported in Table S1.

742 **Table S1.** Resulting fit parameters for c_{ij} and c_{ij}' shown in Figure S4.

743

	c_{ij} (GPa)	c_{ij}'
c_{11}	458(4)	6.1(3)
c_{33}	368(2)	5.7(1)
c_{44}	105(1)	2.1(1)
c_{12}	154(3)	3.3(2)
c_{13}	80(3)	3.7(2)
c_{14}	16(2)	-0.2(1)
c_{25}	-26(1)	-0.6(1)

744

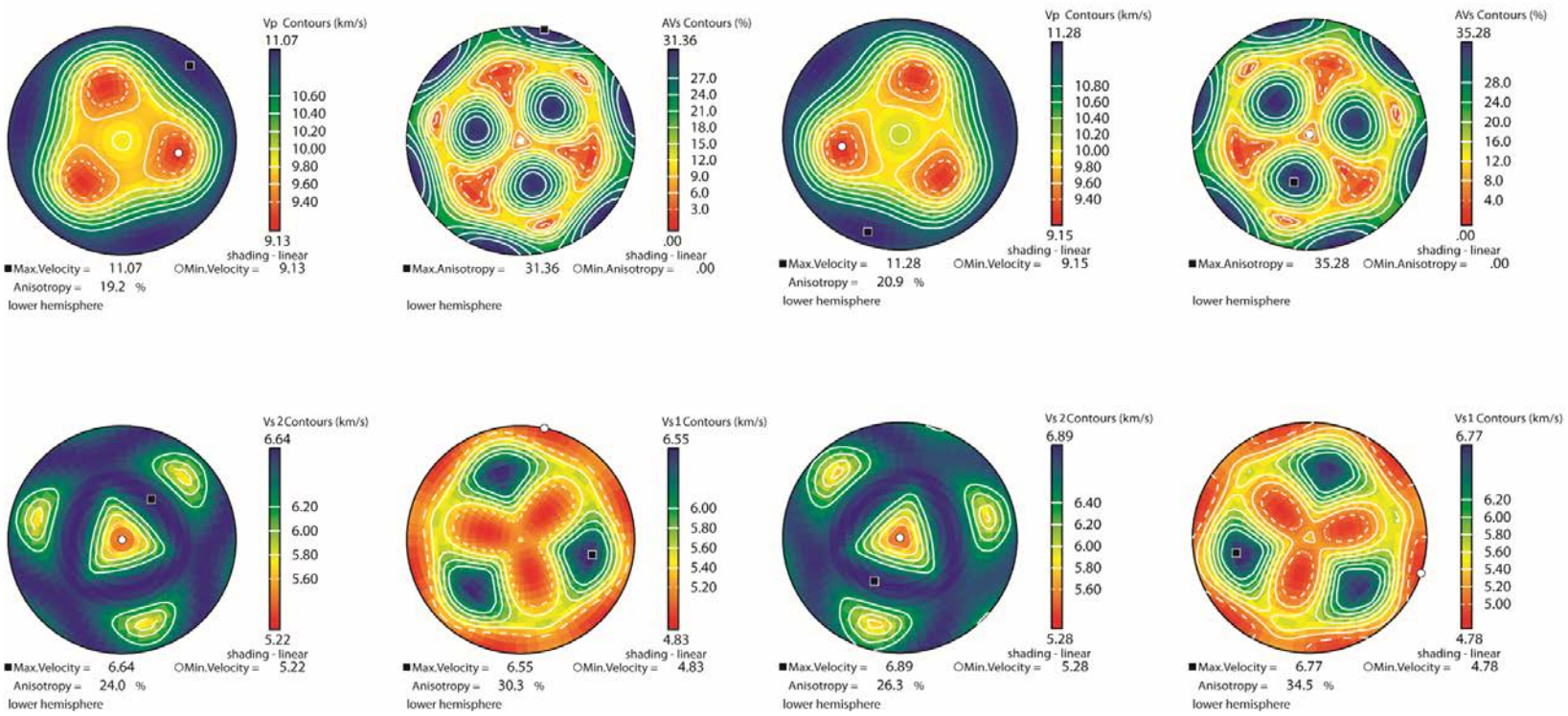

Figure S5. Velocity distributions of $MgSiO_3$ akimotoite at room pressure obtained using the program Anis2k written by Mainprice (1990) using the elastic coefficients determined in this study (left) and Weidner and Ito (1985) (right) and represented in the lower hemisphere. In the lower hemispheres, calculated from the c_{ij} obtained in this study, the crystallographic *a*-axis points towards east (90°) and the *c*-axis points towards the reader. v_P anisotropies (upper left), v_{S1} and v_{S2} anisotropies (lower right and left, respectively), S-wave polarization anisotropy Av_{SP} (upper right). Blue and red colors correspond to the fastest and slowest wave velocities, respectively. The distribution of propagation directions of the P- and S-wave velocities between this study and Weidner and Ito (1985), appears identical except for a rotation of 30° due to a different crystallographic setting used in the mentioned paper.

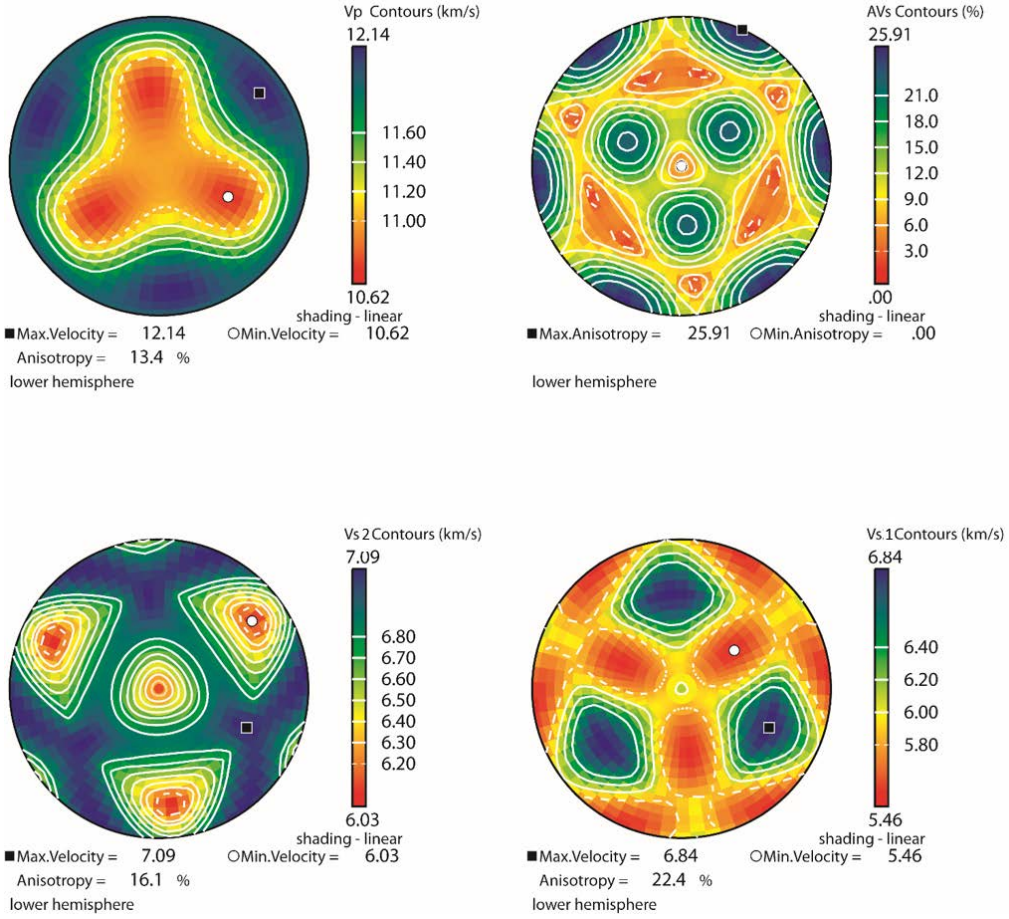

Figure S6. Velocity distributions of $MgSiO_3$ akimotoite at 25 GPa obtained using the program Anis2k written by Mainprice (1990) for the elastic coefficients determined in this study and represented in the lower hemisphere using the same setting as reported in Figure S5. v_P anisotropies (upper left), v_{S1} and v_{S2} anisotropies (lower right and left, respectively), S-wave polarization anisotropy Av_{SP} (upper right). Blue and red colors correspond to the fastest and slowest wave velocities, respectively. With increasing pressure, the P- and S- wave anisotropies decrease; however, the overall velocity distribution remains the same.